Advancing diffusion MRI: improving image quality and getting rid of the fat

Dong, Y.

Chapter 7

Chemical shift encoded multi-shot EPI with structured low-rank reconstruction for Prostate Diffusion-Weighted Imaging

Yiming Dong, David Atkinson, Kirsten Koolstra, Matthias J.P. van Osch, Peter Börnert

Magnetic Resonance in Medicine; under review

Abstract

Diffusion-weighted imaging (DWI) is an important contrast for prostate MRI to enable early and accurate detection of cancer. Single-shot EPI (ssh-EPI) is commonly used for its speed, but often exhibits significant geometric distortions. Multi-shot EPI (msh-EPI) can reduce these distortions and provides better resolution, but suffers from motion-induced, shot-to-shot phase variations. Furthermore, for all EPI-based acquisitions fat signal interference due to the chemical shift effect remains a consistent problem. This study introduces a Dixon-3shot-EPI protocol with structured low-rank reconstruction for efficient prostate DWI, addressing shot-to-shot phase variations and simultaneously allowing water/fat separation. Two raters compared Dixon-3shot-EPI and standard fat-suppressed ssh-EPI (same scanning time) in a cohort of 7 healthy volunteers using a 5-point Likert-scale. From the readers' scores Dixon-3shot-EPI showed significantly less geometric distortion compared to ssh-EPI ($P<0.01$), with no significant differences in other aspects (Prostate Edge Definition / Perceived SNR / Overall Image Quality: $P=0.33/0.09/0.65$). In the quantitative comparison, the ADC values showed no significant difference between the two protocols in all subjects. Dixon-msh-EPI in prostate DWI also offered potential advantages including self-referenced B_0 map-driven geometric distortion correction, more flexibility for increasing the number of slices to be measured or changing TR, increasing spatial resolution, fat-based motion registration, and improved fat suppression, particularly against the olefinic fat peak. In conclusion, Dixon-msh-EPI is a good alternative to ssh-EPI for prostate DWI, allowing a more streamlined scanning scheme and providing reduced geometric distortions with improved fat suppression.

7.1 Introduction

Early detection and accurate characterization of prostate cancer are critical for effective treatment planning and thus improved patient outcomes. As an important MRI contrast, diffusion-weighted imaging (DWI) provides insight into the prostate tissue microstructure by capturing the microscopic mobility of water molecules. Consequently, DWI forms a key element of the diagnostic pathway for suspected prostate cancer[139].

Single-shot EPI (ssh-EPI) is often preferred for clinical prostate DWI due to its speed and simplicity[9]. Using magnitude signal averaging in the image domain, DW ssh-EPI can mitigate artefacts due to the strong motion sensitivity of the diffusion sensitizing gradients causing image phase inconsistencies between individual shots[62]. Whereas many clinical studies have been performed using DW ssh-EPI[9,140–142], the proximity to the rectum can cause severe local susceptibility artefacts and distortions, especially in the presence of gas or stool[37,61,89,143]. Moreover, the long readout time of ssh-EPI may limit the achievable spatial resolution[39]. As an alternative, multi-shot EPI (msh-EPI) techniques have been introduced allowing for an increased phase-encoding bandwidth, resulting in significantly reduced geometric distortions and shorter TE, enabling thus potentially higher spatial resolution[39,48,51,144]. Recently, such benefits of msh-EPI have been validated in prostate[145] and female pelvis[118] DWI studies. However, a key challenge for msh-EPI is to efficiently and effectively correct for the physiological motion-induced shot-to-shot phase variations[32]. Several approaches have been proposed to address this issue, including the use of additionally measured phase navigators[39], self-navigation-based phase-estimation[47,48], and the use of structured[51,52,119] or locally low-rank[49,50] matrix completion.

Regardless of whether ssh- or msh- EPI is used, fat signals are often a confounding factor due to the low diffusivity and short T1 which, if unsuppressed, results in fat appearing bright in DWI[41,75]. The chemical shift effect further complicates matters by shifting fat signals along the EPI phase encoding direction, which can obscure tumor visibility, especially when attenuated water signals are obscured by the displaced fat signals[41,77]. Therefore, effective fat suppression is essential for EPI-based DWI. While SPectral Attenuated Inversion Recovery (SPAIR[73]) is a common choice in prostate DWI[11,143,146,147], it may fail, like other spectral selective fat suppression approaches, where B_0 offsets are severe[41,76,115]. Furthermore, the use of additional fat-saturation pulses may compromise scan efficiency, especially when acquiring more slices or higher through-plane resolution are required in a clinical setting.

In our earlier work, a combination of chemical shift encoding with diffusion weighed msh-EPI (Dixon-msh-EPI) was introduced with associated data-driven, navigator-free reconstructions to simultaneously address shot-to-shot phase variations and fat signal interference[148]. The idea was to complement the core attributes of msh-EPI with appropriate TE shifts to facilitate Dixon-encoding, avoiding the need for additional fat suppression pulses to remove the fat. This prevents affecting the vulnerable water magnetization, which is especially relevant for high b-value, diffusion weighting.

The primary objective of this study is to evaluate the performance of Dixon-msh-EPI as an alternative to standard fat suppressed ssh-EPI for prostate DWI. Both techniques are compared in quantitative and qualitative manners in a healthy volunteer cohort using protocols with similar total scanning time while acquiring four b-values between 0 and 1000 s/mm^2.

In addition, this study explores other advantages of the Dixon-based water/fat separated DWI msh-EPI technique, like the possibility of correction of residual EPI geometric distortions using the Dixon B_0 map, improved opportunities for cross b-value registration by using the fat images, and improvement of fat suppression, particularly of olefinic peak signals.

7.2 Methods

7.2.1 Reconstruction and post-processing steps

Chemical shift encoding is a robust technique for estimating water, fat images, and a B_0 map simultaneously, by acquiring data at multiple ΔTEs to encode phase changes induced by fat and B_0 off-resonances[56,58,81,85,149]. To integrate Dixon with msh-EPI for DWI, additional constraints are required for an appropriate reconstruction. The MUSSELS algorithm, proposed for the reconstruction of fat-suppressed DW ms-EPI images, introduces the Hankel matrix into the reconstruction pipeline. This navigator-free approach could help to reconstruct phase-corrected DW images from each shot of under-sampled multicoil measurements by exploiting the across-shot data low-rank property[51,52]. To reconstruct the DW image while correcting for shot-to-shot motion-induced phase variations, two individual Hankel matrices[51,52,148] can be used as constraints for the water/fat components, respectively. Those guide the complex-valued water/fat image separation. Prior to b>0 s/mm^2 image reconstruction, a B_0 map can be estimated from the b=0 s/mm^2 images, because these do not exhibit motion-induced phase errors. The cost function for the b>0 s/mm^2 reconstructions can be written as:

$$\{P_w, P_f\} = \underset{\hat{x}_w, \hat{x}_f \in \mathbb{C}^{Q\times N\times L}}{\operatorname{argmin}} \|AP - d\|_2^2 + \lambda_1 \|H(FP_w)\|_* + \lambda_2 \left\|H\left(FP_f\right)\right\|_*, \tag{1}$$

where $P = [P_w, P_f]^T = [\rho_{w,1,1}, \dots, \rho_{w,N,1}, \dots, \rho_{w,1,L}, \dots, \rho_{w,N,L}, \rho_{f,1,1}, \dots, \rho_{f,N,1}, \dots, \rho_{f,1,L}, \dots, \rho_{f,N,L}]^T$ represents the reconstructed complex-valued water and fat images with L shots and N Dixon points, d is the measured data and A is the model-based water/fat separation system matrix described in refs.[115,148]. The two regularization terms ($H\left(FP_{w/f}\right)$) provide two structured low-rank constraints in k-space on the water and fat channels, respectively. These help the reconstruction to use the redundant magnitude information between all the different "repeatedly" measured data of the same subject (multiple shots/Dixon points), while also reconstructing the phase of each individual shot. We refer interested readers to the original papers[51,52,148] for more details.

7.2.1.1 Complex-signal averaging

DWI is a technique that suffers from low SNR, because the moving water signals are attenuated during the diffusion sensitizing gradients. Therefore, signal averaging is often recommended, which is especially important for SNR-critical prostate high b-value DWI[140,145,150]. A natural advantage of solving Eq. 2 is that both the data consistencies and the regularizations are implemented in a complex manner with associated complex signal averaging between iterations. This concept is consistent with the post-processing phase correction step described in earlier work to restore "real" DWI signals while preserving the Gaussian noise distribution[151,152]. Complex averaging is also of benefit to ssh-EPI reconstructions to avoid the non-zero-mean Rician noise that is present when magnitude averaging is used. Thus, after reconstructing the individual complex ss-EPI images and exporting their phase maps $\hat{\phi}(x, y)$, a spatial low-pass filter (e.g., a 5×5 square convolution kernel [152]) can be applied for smoothing the phase maps followed by a phase correction using a complex rotation:

$$\rho_c(x, y) = \rho(x, y)e^{-i\hat{\phi}(x,y)}, \tag{2}$$

and final signal averaging[152]. Supporting information Figure S.1 gives a comparison between absolute-value-averaging and complex-averaging in DW ssh-EPI.

In this study, and based on the previous work from literature [10], it's assumed that prostate tissue shows mainly isotropic diffusion. Therefore, signals from all different directions were directly averaged, reconstructing a single combined image for each b-value. Direction-specific, eddy current- induced, geometric distortions were ignored and not corrected.

7.2.1.2 B_0 map-based geometric distortion correction

In EPI sequences, signals displaced by geometric distortions can be restored to their original locations by modeling the point spread function in conjunction with the associated B_0 field map[37,61,89]. An additional B_0 map estimation[143,147] scan can be recorded to facilitate such corrections[61,89,143]. However, such a B_0 map acquired as pre-scan can quickly become “outdated” in prostate MRI due to local susceptibility variations, e.g., due to changes in the nearby rectum[147], and potential scanner center frequency shifts. In case of Dixon-msh-EPI, an estimated B_0 map is already available from the b=0 s/mm^2 data water/fat separation. Although the geometric distortions are already reduced in msh-EPI compared to ssh-EPI, the B_0 map-information could still be used to further correct for residual geometric distortions. A straightforward and efficient approach uses the Conjugate Phase Reconstruction (CPR)[88,99] method.

7.2.1.3 Fat-based registration

The presence of fat signals in DW-EPI images is undesirable because of its low diffusivity. This results in bright fat signal and chemical-shift displacements which might obscure important water tissue. Conversely, fat can serve as a valuable reference for tracking macroscopic motion, as for example demonstrated in brain studies using an extra fat-selected navigator[133,153]. In Dixon-msh-EPI, fat images are estimated for each reconstruction, providing a potential basis for estimating macroscopic motion parameters which can subsequently be applied to the water images for correction. This is particularly important in scenarios involving high-b value, low-SNR, DW water images (e.g., the b=1000 s/mm^2 component used for calculating ADC), where direct water-based registration might pose significant challenges.

7.2.2 MRI technique

All experiments were performed using a 3T scanner (Philips Healthcare, Best, The Netherlands). A total of 7 healthy male volunteers were included in the study, informed consent was obtained according to the rules of the Institutional Ethics Review Board. All were scanned using a baseline prostate multi-slice 2D T2w TSE protocol (TE/TR=110/2000ms, in-plane resolution 0.4×0.71mm^2) followed by two DW scans, an ssh-EPI and a Dixon-msh-EPI. To facilitate a comparison, the basic scan parameters of the used single-shot EPI and the Dixon-3shot-EPI protocol were matched regarding the same in-plane resolution (1.6 mm^2), half-Fourier scan parameter (0.632), number of slices (12), and slice-thickness (3 mm). The effective number of signal averages (eNSA), here defined as the number of excitation pulses or EPI-signal read-out trains used, was matched for the highest b-value (b=1000 s/mm^2) between the two DWI protocols. Thus, 4 b-values (b=0, 150, 500, 1000 s/mm^2) were acquired for both sequences with eNSA = 4, 12, 24, 36 for ssh-EPI and eNSA=9, 9, 18, 36 for msh-EPI. The discrepancy in signal averaging of lower b-values (b<1000 s/mm^2) enabled us to match the scan time of the msh-EPI to the ssh-EPI scan (both ~5 min). The impact of the eNSA discrepancy on SNR for the lower b-values is not evaluated in this study. It should be remembered that we assume that the prostate is an isotropic tissue, as shown in ref.[10] (see section 2.1) and therefore all directions are combined when performing signal averaging for each b-value, and a maximum of 4 diffusion directions were measured. For all Dixon-msh EPI scans, three Dixon points were chosen, shifted with respect to the spin-echo by 0.2ms, 1.0ms, and 1.8ms, respectively. All other scan parameters for the base protocols of ssh-EPI and Dixon-msh-EPI are listed in Table 1. The fat-suppressed (SPAIR) msh-EPI data were also measured with 4 b-values (b = 0, 150, 500, 1000 s/mm^2) and eNSA = 9, 9, 18, 36. In addition, several other scans with different parameters were performed for the msh-EPI to study the dependency on different scan parameters, see "additional scans" in Table 1.

All reconstruction pipelines were implemented in Python 3.8. The ssh-EPI images were reconstructed by a basic SENSE[30] pipeline for each measurement. Additional phase correction with real data averaging was performed for each b-value according to the method[152] (see Section 2.1.1). For the reconstruction of Dixon-msh-EPI (it will be referred to as Dixon-3shot-EPI in the Results section), the structured low-rank reconstruction pipeline of our original paper[148] was slightly modified to fit the low-SNR prostate data as follows: The "magnitude-averaging" step[32] is now performed among all different Dixon points/shots/diffusion directions for each b-value, ignoring any pixel misregistration in image space. The hyperparameters were also chosen to be slightly different from the original work, with empirical choices of: (1) a window width of 1/4 of the image matrix size for the triangular filter, applied after each iteration to enforce the smoothness of the phase map, and (2) regularization factors $\lambda_1 = 0.0015$ for the water and $\lambda_2 = 0.00025$ for the fat channel. For the quantitative and qualitative comparison between the two base protocols, CPR for further geometric distortion correction was not applied. The fat-suppressed (SPAIR) 3shot-EPI data were reconstructed using a modified IRLS-MUSSELS[52] algorithm, with a chosen regularization factor of 0.002, which reconstructs all diffusion directions/shots jointly. For the fat-based registration comparison, a combined registration pipeline with (1) a rigid motion registration, (2) followed by a diffeomorphic field[154] nonlinear registration was used, applying the correction subsequently to the corresponding images. The implementation was based on the python package Dipy[155] .

Table 1. sequence parameters.

sequence	fat suppression	resolution (mm^2)	scan time (min:sec)	FOV (mm^2)	TE / TR (ms)	bandwidth in phase-encoding (Hz/pixel)
base protocols						
ssh-EPI*	SPAIR	1.6×1.6	5: 08	220 x 168	82 / 4000	9.1
Dixon-3shot-EPI	Dixon	1.6×1.6	5: 00	250 x 230	54 / 4000	20.4
additional scans						
Dixon-3shot-EPI	SPAIR	1.6×1.6	4: 56	250 x 230	54 / 4000	19.4
Dixon-3shot-EPI	Dixon	1.6×1.6	5: 00	250 x 230	57 / 4000	16.5
Dixon-3shot-EPI	Dixon	1.6×1.6	3: 45	250 x 230	54 / 3000	20.4

*based on a clinical protocol from the University College London (slightly modified)

7.2.3.1 Quantitative image analysis

Quantitative comparison was performed by comparing ADC values and apparent SNR (aSNR) of the two base protocols (ssh-EPI and 3-shot-EPI). The ADC maps were derived pixel-wise using a linear fit to the logarithm of the signal values from the four b-values. The ADC values are reported as the mean and standard deviation within the ROIs. The ROIs for each technique were placed in the transition zone regions, free of signal pile-up to avoid potential biases induced by susceptibility-related artifacts. For each subject, 6 central slices were included in the ADC analysis. ADCs from the two techniques were compared using a paired t-test with P-value < 0.05 considered as statistically significant.

The aSNR was calculated as the ratio between the mean signal intensity within an ROI and its standard deviation. The ROIs were selected according to the same procedure as for the ADC analysis, except that only a single central slice was selected for each subject. The aim was to cover the maximum number of pixels of homogeneous tissue in the transition zone area.

7.2.3.2 Qualitative image analysis

The qualitative image analysis was performed by two MRI experts, both with several years of experience in interpreting MRI images (prostate and other anatomies). The images acquired and reconstructed were arranged as sets, each comprising of all four b-values. A total of 92 sets were scored (46 for ssh-EPI and 46 for Dixon-3shot-EPI). All sets were presented in random slice and MRI sequence order in a double-blind manner to the two readers, who judged the image quality based on a 5-point Likert scale[150] along four different scoring dimensions:

a. Geometric distortion (1: no; 2: low; 3: intermediate; 4: high; 5: very high)

b. Prostate edge definition (1: poor; 2: below average; 3: average; 4: above average; 5: clear)

c. Perceived SNR (1: very low; 2: low; 3: average; 4: high; 5: excellent)

d. Overall image quality (1: poor; 2: below average; 3: average; 4: above average; 5: excellent)

Qualitative scores were compared between the two base protocols by means of a Wilcoxon signed-rank test, with a P-value < 0.05 considered as statistically significant. The inter-rater agreement between two readers was assessed using the Kendall τ test.

7.3 Results

7.3.1.1 quantitative comparison between Dixon-3shot-EPI and ssh-EPI

ADC [$\times 10^{-3}$ mm^2/s] (Dixon-3shot-EPI)	ADC [$\times 10^{-3}$ mm^2/s] (ssh-EPI)	P-value	aSNR (Dixon-3shot-EPI)	aSNR (ssh-EPI)
1.25 ± 0.36	1.28 ± 0.30	0.056	7.29	8.76
1.54 ± 0.25	1.54 ± 0.27	0.499	8.92	12.49
1.21 ± 0.25	1.19 ± 0.27	0.230	5.82	6.51
1.28 ± 0.20	1.25 ± 0.23	0.053	9.01	9.37
1.26 ± 0.27	1.29 ± 0.36	0.181	8.28	9.88
1.22 ± 0.24	1.25 ± 0.30	0.062	8.81	10.40
1.31 ± 0.22	1.32 ± 0.27	0.714	10.15	12.25

Table 2. The quantitative measures of ADC and aSNR for Dixon-3shot-EPI, ssh-EPI and each subject. ADC values were calculated from all 6 ROIs for each subject for each technique, and the corresponding p-values were determined between the two techniques in terms of ADC.

Results of the quantitative measurements are shown in Table 2 for each subject and each technique. There was no significant difference in ADC values between the two techniques ($P > 0.05$). The apparent SNR for complex averaged ssh-EPI was found to be higher than that for Dixon-3shot-EPI.

3.1.2 qualitative comparison between Dixon-3shot-EPI and ssh-EPI

	Dixon-3shot-EPI	ssh-EPI	P-value
Geometric distortion	1.54 ± 0.83	2.00 ± 1.20	0.032
Prostate edge definition	3.98 ± 1.13	3.76 ± 1.16	0.078
Perceived SNR	3.91 ± 0.78	4.11 ± 0.79	0.007
Overall image quality	4.02 ± 0.79	3.91 ± 0.90	0.631

Table 3. Qualitative comparison between Dixon-3shot-EPI and ssh-EPI. Aggregated average scores + standard deviation are reported for two readers, each of whom independently scored 92 different sets.

The results of the qualitative comparison between the two techniques by two readers are shown in Table 3. There was significantly less geometric distortion in Dixon-3shot-EPI compared to ssh-EPI ($P<0.01$), whereas there was no significant difference in all other aspects between the two techniques (Prostate Edge Definition / Perceived SNR / Overall Image Quality: P=0.33/0.09/0.65). The Kendall τ correlation indicates good reader agreement for most aspects of ssh-EPI (τ = 0.50/0.56/0.71 for Geometric Distortion/Prostate Edge Definition/Overall Image Quality, all $P < 0.01$) and Dixon-3shot-EPI (τ = 0.68/0.57/0.63, all $P < 0.01$). However, for Perceived SNR, ssh-EPI shows good agreement ($\tau = 0.56$, $P < 0.01$), while Dixon-3shot-EPI shows moderate agreement ($\tau = 0.39$, $P < 0.01$).

7.3.2 Geometric Distortion reduction

Figure 1 (A) and (B) show images of two different slices of one volunteer, obtained using the base protocols (ssh-EPI, and Dixon-3shot-EPI) with two additional T2w TSE images for reference as well as the calculated ADC maps. The Dixon-3shot-EPI images were further post-processed with CPR for further geometry correction. Furthermore, the corresponding fat images obtained from the Dixon-3shot-EPI are shown as an additional contrast for radiological interpretation. The lower geometric distortion of Dixon-3shot-EPI compared to ssh-EPI is clearly visible, especially when comparing the data to the corresponding T_2 weighed TSE scan. Furthermore, additional geometric distortion corrected data are shown, i.e. after applying CPR. The water-fat merged T_2w images may provide an alternative option for visual-reference or image-registration algorithms to spatially align the high-resolution T2w FSE images with distorted DWI. It should be noted that, based on the complex averaging property of the reconstruction pipeline for Dixon-3shot-EPI data, and the additional post-processing of the ss-EPI data no Rician noise bias was induced into the ADC calculation.

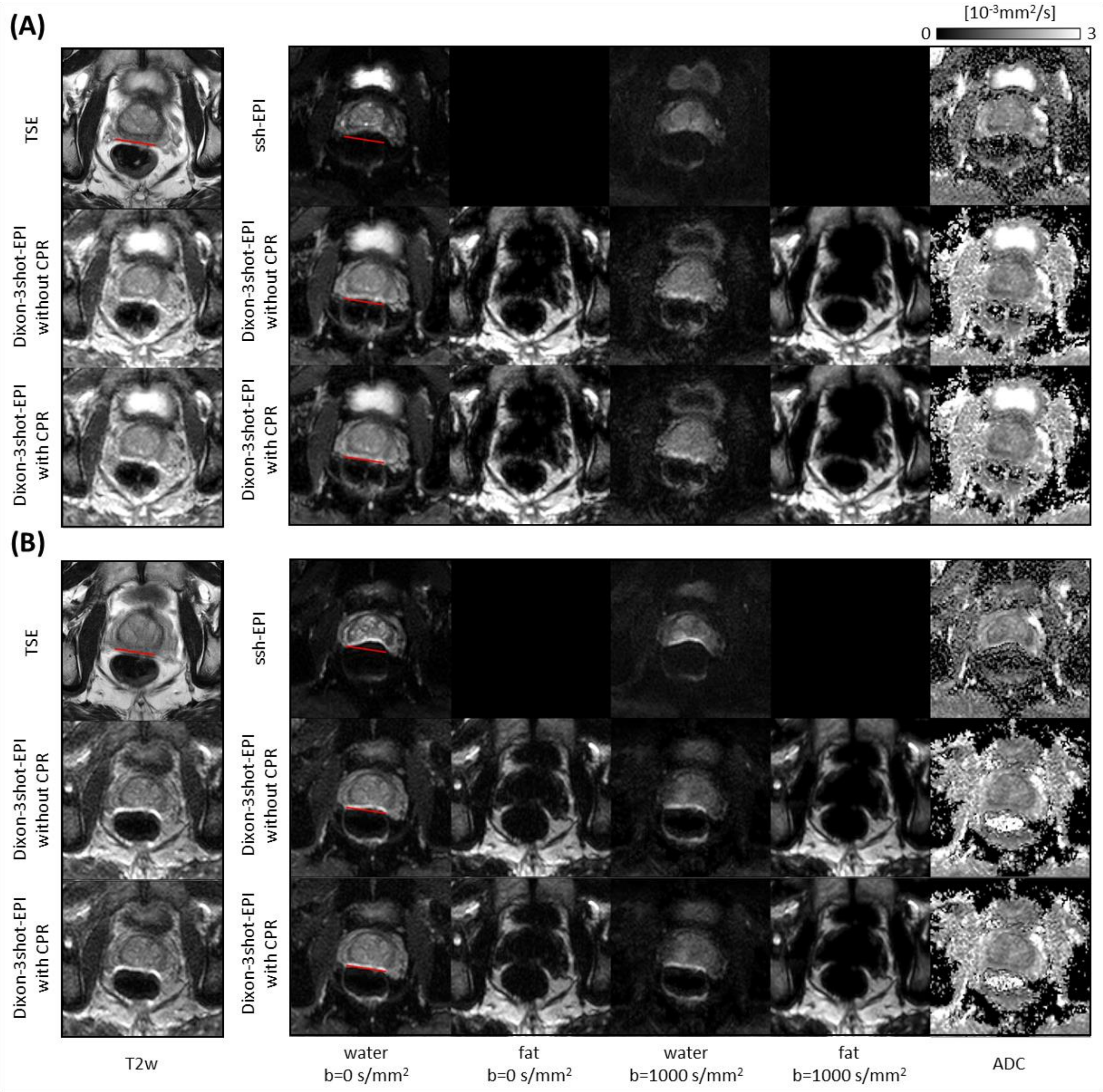

Figure 1. Comparison of three techniques (ssh-EPI, Dixon-3shot-EPI without CPR and with CPR). Prostate DW images (b=0 s/mm^2 and b=1000 s/mm^2) for two slices of one volunteer are given. The left columns of (A) and (B) show the corresponding fat-unsuppressed T_2w TSE images for anatomical reference, along with water/fat merged b=0 s/mm^2 images from the Dixon-3shot-EPI for comparison. The right part of (A), (B) show a comparison between the 3 techniques (Dixon-3shot-EPI with / without CPR and ssh-EPI) and the corresponding ADC maps. No fat images for the ssh-EPI are available due to the use of SPAIR. The increased bandwidth along the phase-encoding direction of the Dixon-3shot-EPI results into less geometric distortions for both slices and b-values. In addition, the B_0 map estimated from the Dixon data can directly be used to further correct "remaining" geometric distortions via a conjugate phase reconstruction (CPR). Note, the red reference lines from the T_2w TSE help the eye to judge the geometric distortions on the water DWIs (only added to b=0 data).

7.3.3 Shorter TR

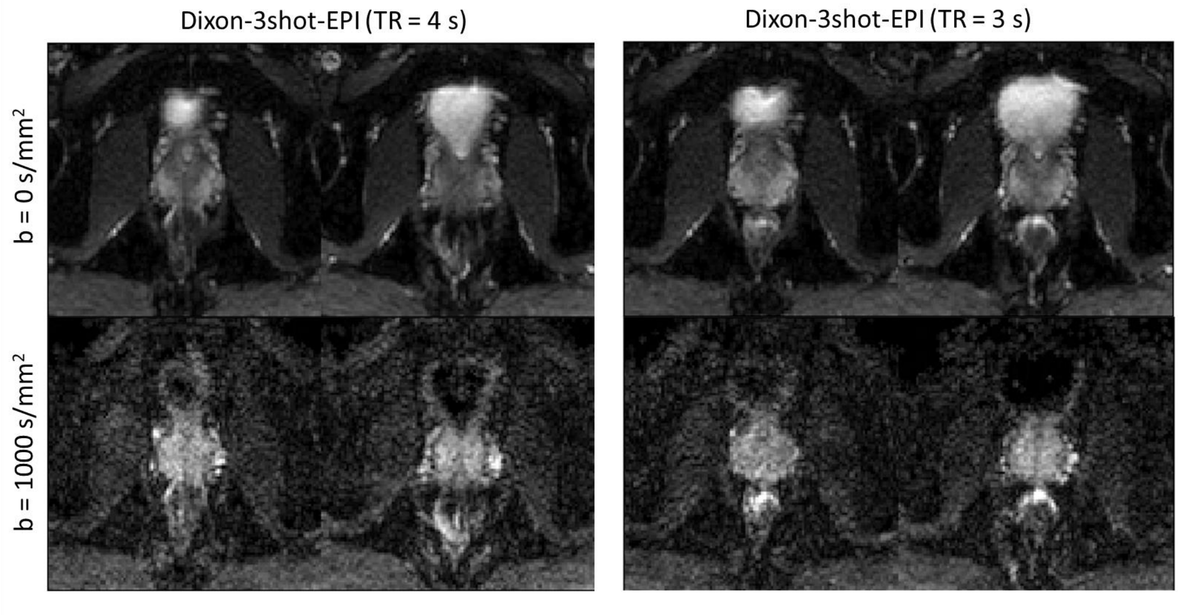

Figure 2. Comparison of prostate DWI results of one subject measured with two different TRs. The apparent SNRs for b=1000 s/mm^2 are 9.00 and 7.73 for TR = 4s and 7.49 and 7.11 for TR = 3s. This slight SNR drop can be explained by less T_1 recovery for the TR 3s case.

Figure 2 shows a comparison between two scans of the same subject but with different TR. There is a slight loss of SNR when the TR was decreased (from 4 s to 3 s), which is consistent with basic MR physics taking the prostate T_1 into account. However, the total scan time was reduced by more than one minute, which can be considered significant in a clinical setting (Table 1). Scan efficiency is especially crucial for prostate scans, as peristaltic motion can occur as well as changes in bladder shape as one can clearly see in Figure 2, even though the two images were taken immediately after each other.

Note, that with the current scan settings, both ssh-EPI and 3shot-EPI cannot acquire all 12 slices within a single TR package (3s) when using SPAIR-based fat suppression. This means that either less slices or a longer total scanning time must be accepted compared to the Dixon-msh-DW EPI approach.

7.3.4 High-resolution DWI for prostate

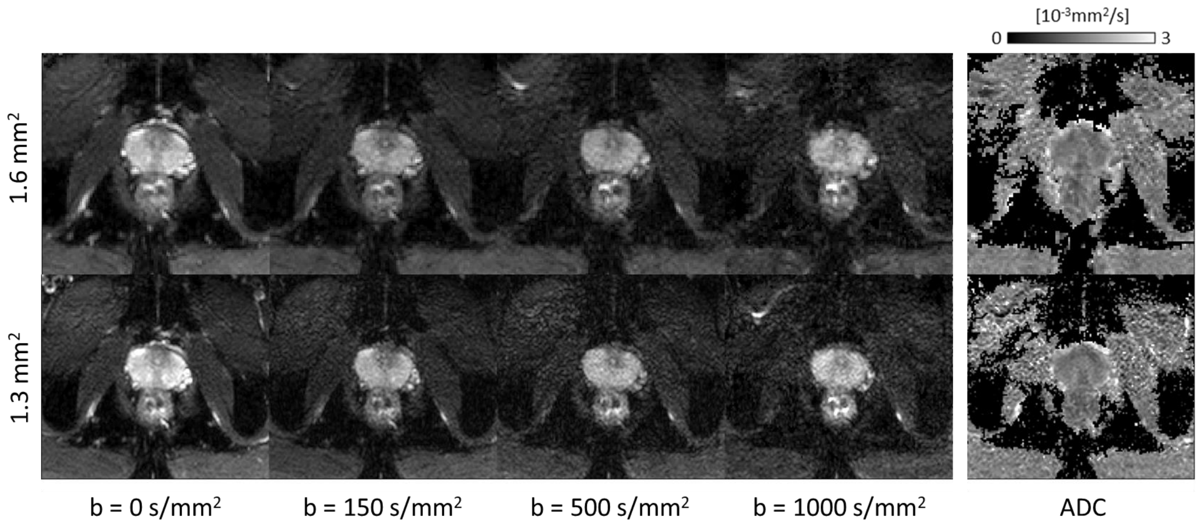

Figure 3. Comparison of Dixon-3shot-EPI DWI images acquired at different in-plane resolution. A selected slice of a subject's prostate is shown. Four b-values along with the corresponding ADC maps are given for a 1.6 mm (top row) and 1.3 mm (bottom row) in-plane resolution scan, respectively. The 1.3 mm in-plane resolution images show improved sharpness in the inner prostate structures and in surrounding muscle tissue compared to the slightly lower resolved ones.

A notable advantage of msh-EPI is that the shorter readout window allows for higher resolution. Figure 3 shows prostate images of a subject with an in-plane resolution of 1.6 mm and at a slightly higher resolution of 1.3 mm. The improvement in resolution can be seen, although there is also a noticeable loss in SNR since the scanning time was kept almost untouched. However, the gain in resolution can be appreciated in the ADC maps.

7.3.5 Fat-navigator for registration

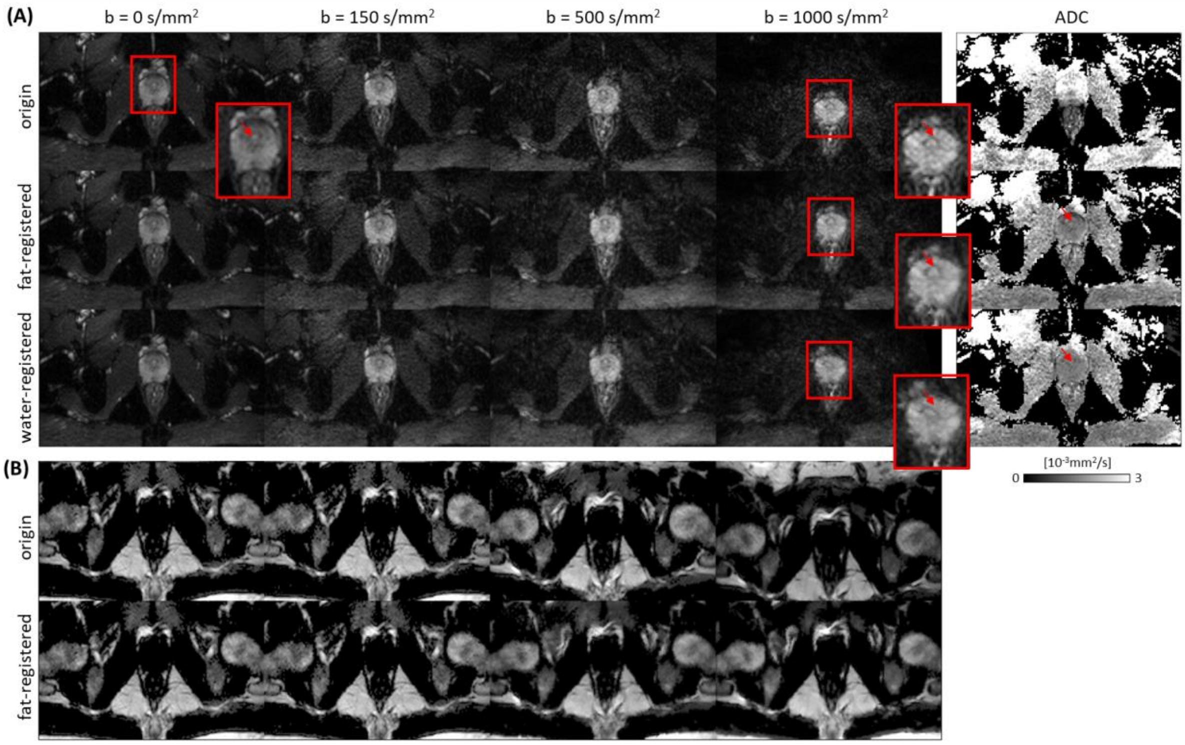

Figure 4. Provoked gross motion and cross b-value registration (macroscopic motion-correction). Data from a selected slice of one subject's prostate are shown for four b-values. (A) shows water DWI, (B) fat DWI data. The top row in (A) shows original data, with the corresponding ADC map on the right. In the next rows two different registration approaches have been used: (1) using fat images for registration (fat-registered), and (2) directly registering the water images (water-registered). The original images were acquired with the subject asked to move between the different b-value acquisitions in the anterior-posterior direction, and this motion was assisted by removing support-pads. A clear spatial mismatch can be seen in both water and fat images. When the fat images were used as input for the registration, the inner structure is registered nicely as shown by the red arrow, while direct registration from water did distort the inner structure (red arrows) and generated blurring in the final water ADC maps.

Figure 4 shows a prostate scan of a subject who was requested to slightly move the body during the b = 500 s/mm^2 and b = 1000 s/mm^2 scans to simulate some macroscopic motion-induced in-plane inconsistencies. The reconstructed images were (1) fat registered by estimating motion parameters through the reconstructed fat images for each b-value, and (2) water registered by directly estimating the motion parameters for the water images of each b-value. A deformation can be observed in the water-registered case as marked by red arrows, mainly due to the low SNR in the b=1000 mm^2/s water image for the non-linear registration.

7.3.6 Fat-suppression

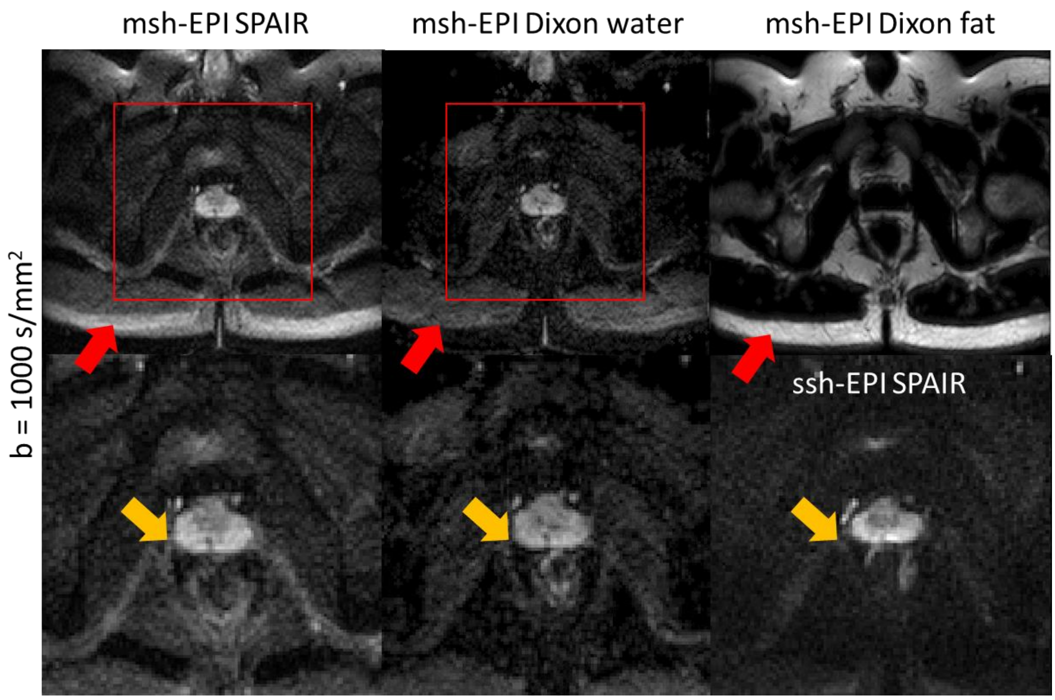

Figure 5. Prostate DWI using 3shot- and ssh-EPI and different fat suppression or separation approaches. Images (b=1000s/mm²) from a selected slice of one subject are shown. The first row shows SPAIR-fat suppressed 3shot-EPI (water) and Dixon-3shot-EPI (showing water and fat separately) in their original FOV. Some unsuppressed fat signals from the posterior region can be seen that have moved up to cover the muscle tissue. Whereas the Dixon method does a better job suppressing those signals (indicated by the red arrows). The second row provides zoom-ins. The first 3shot-EPI images (from the red squares above) are acquired at TE = 54ms, next to an ssh-EPI image acquired at TE = 82ms. Due to the T_2 relaxation, the problematic olefinic fat signals have faded to noise level in the ssh-EPI and don't interfere with the prostate tissue signal. In comparison, at the shorter TE, some fat signals are still present in the center of the 3shot-EPI + SPAIR image, covering the prostate (yellow arrows). However, this can be avoided by employing Dixon-3shot-EPI.

Figure 5 shows a comparison between 3 approaches of fat suppression. The most difficult peak for fat-saturation techniques such as SPAIR, is the olefinic peak which is close to the water resonance (~0.61 ppm). Such an unsaturated fat artefact caused by olefinic signal can be appreciated in the b=1000 s/mm^2 msh-EPI SPAIR data. However, it can be nicely separated by Dixon since the signals are chemical shift encoded and a proper multipeak fat spectrum model can be employed. Note that due to the short T_2 of this peak (38.7 ms), the olefinic signal has already dropped into the noise level for ssh-EPI with a typical TE of 82 ms. However, when acquiring data at TE = 54 ms with msh-EPI, it can be clearly observed.

In addition, in the ssh-EPI with SPAIR in one subject, a failure of fat suppression was observed, mainly due to severe B_0 inhomogeneities, as shown in Supporting Information S.2.

7.3.7 ADC mapping

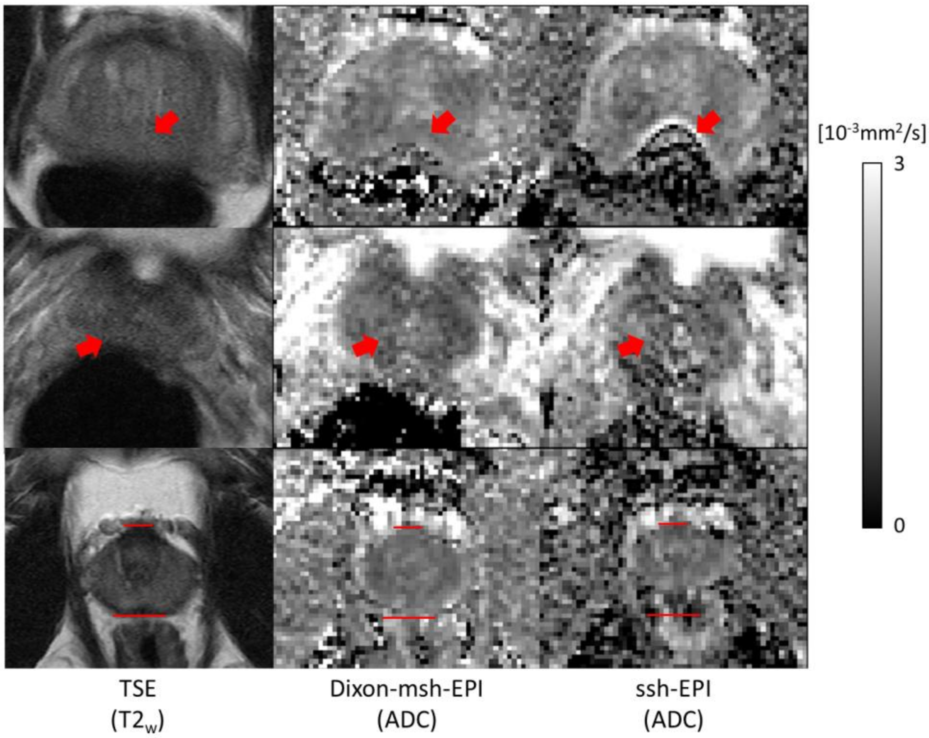

Figure 6. Prostate T_2w TSE images and corresponding ADC maps measured with Dixon-3shot-EPI and ssh-EPI. Selected data of three volunteers are given highlighting imaging problems. TSE images are shown for anatomical reference. In the first volunteer (top row), signal pile-up in ssh-EPI causes an erroneous ADC mapping with abnormally high ADC values (marked by red arrows), whereas Dixon-3shot-EPI can significantly reduce such errors. In the second volunteer (middle row), Dixon-3shot-EPI is less sensitive to the susceptibility artifacts (red arrows) and provides more stable ADC mapping compared to ssh-EPI. In the last volunteer (bottom row), although no dramatic artifacts can be seen in the ssh-EPI ADC map, the Dixon-3shot-EPI shows a better match with respect to position and shape of the prostate along the phase encoding direction when compared to the TSE image (marked by a pair of red bars).

Figure 6 shows ADC maps of Dixon-3shot-EPI and ssh-EPI from three slices of three different volunteers. Compared to the TSE T2w images as anatomical reference, ssh-EPI shows severely degraded ADC mapping in certain regions (red arrows), mainly due to the geometric distortion induced by the inhomogeneous B_0 field around air-tissue boundaries. In contrast, Dixon-3shot-EPI provides better ADC mapping at the corresponding regions.

7.4 Discussion

This study showed that Dixon-msh-EPI significantly outperformed ssh-EPI in reducing geometric distortions, mainly caused by the presence of bowel gases, improving the potential diagnostic value at the expense of a slight loss in SNR for the same scanning time. When scoring overall image quality, the Dixon-msh-EPI was qualitatively on a par with ssh-EPI for diffusion weighted prostate imaging. The direct access to fat in Dixon-msh-EPI, offers additional advantages enabling the use of fat as a navigator for gross motion correction and as additional diagnostic information. With the help of the chemical shift encoding concept and the data driven shot-phase navigation, the DW Dixon-msh-EPI sequence performs diffusion and chemical shift encoding simultaneously in an efficient and compact manner.

Quantitative prostate ADC assessments demonstrated a high agreement between the two EPI methods, with no statistically significant difference. Comparing the SNR, the ssh-EPI showed a slightly higher mean aSNR (<14%), for the same, fixed total scanning time. In this context, for both sequences similar effective NSAs (eNSA) were used for the individual b-values (defined as the number of EPI read-out trains following 90° excitation). The shorter total acquisition window of msh-EPI compared to ssh-EPI resulted in a SNR loss, which was only partly compensated by the higher signal at shorter TE (healthy prostate T_2: 90~140 ms[156]). Thus, the expected theoretical SNR loss can be calculated to be around 10% for msh-EPI, which matches the calculated results (Table 2). However, the observers found this difference in perceived SNR, between the two protocols, to be statistically insignificant (Table 3).

Beyond the observer comparison, we also investigated other advantages of Dixon-msh-EPI over ssh-EPI for prostate DWI. A primary advantage is the use of the simultaneously obtained B_0 map to further correct for remaining geometric distortions (see Figure 1). The B_0 map derived from the chemical shift encoded b=0 s/mm^2 data, is acquired along with the actual EPI scan and reflects therefore intrinsically the actual scan conditions (off-resonance, sampling bandwidth, motion state, etc.) [88,99]. However, when signal pile-up artifacts become visible, blip-up/blip-down approaches[143,147] might offer potentially an alternative solution, but also there a pre-measured B_0 map can become outdated[147], suggesting that a Dixon-derived one will still be useful[157]. Furthermore, the Dixon approach with the separated water and fat channel allows for retrospective image fusion. Thus, chemical shift-corrected water fat merged Dixon-msh-EPI images could be formed (Figure 1) to give radiologists a valuable reference to visually align or to register the still geometrically distorted DWI EPI scans with the geometric-distortion-free TSE T_2w images to ease reading and evaluation.

In addition, the fat images might be of benefit for motion correction. For example, in ADC mapping, cross-b-value registration is always challenging due to the low SNR for high water b-values (see Figure 4). In contrast to the water, the fat signal does not change much as a function of the b-value due to low fat molecule mobility. Therefore, the fat signals can serve as good motion trackers by exploiting the periprostatic fat surrounding the organ. The presented fat-based registration along different b-values is just a proof of concept, which could be extended further to correct macroscopic motion between different Dixon points or shots while performing the reconstruction. Even small eddy current effects, caused by the switching of the strong diffusion sensitizing gradients applied in different directions, can manifest as slight geometric distortions in the images, might be corrected this way. It is important to note that, in this initial test, only in-plane motion correction has been addressed, which could lead to errors in ADC mapping due to a mismatch in prostate tissue structure between b-values. In the future, through-plane motion correction using fat signals may be further explored, and the advantages achieved with the Dixon (potentially higher resolution in the slice direction) may be helpful in this case.

Apart from the ability to use the fat to track and correct for macroscopic motion-related effects during the DWI scan, the fat might also be of diagnostic value. Fat plays a role in many biological processes including cancer and other pathology[57]. Early research suggested that periprostatic fat thickness can have a relation to prostate cancer[158–160]. Thus, the use of Dixon-EPI approaches that provide access to fat might be interesting from this angle.

It is known from skeletal muscle DWI, that the signal from the olefinic fat peak, which is close to water, and which therefore cannot easily be suppressed by SPAIR, is often confounding image quality[14,78]. In prostate DWI, the olefinic signal from the periprostatic fat, when present, can cause artifacts in short TE measurements (e.g., msh-EPI with TE < 60 ms). It can be shifted in the phase encoding direction and might overlap prostate tissue (c.f. Figure 5). This phenomenon has not been previously described, probably because the routinely used ssh-EPI with its relatively long TE (~82 ms, in this work), may already cause substantial T_2 relaxation, making this peak signal (T_2 ~38 ms at 3T [54]) drop into the noise floor.

The results of this study highlight a quantitative consistency and reproducibility between the two protocols, particularly in regions where geometric distortion is absent. In the current study, the Dixon-msh-EPI was measured with 3 shots, while using more shots could potentially further minimize geometric distortion and reduce TE, but at the expense of either longer scanning times[32] or slightly impaired SNR. Longer scanning times could be circumvented by appropriate under-sampling of the Dixon-shot encoding space[148]. However, as an initial Dixon-msh-EPI study for prostate, the major aim was to compare the Dixon-msh-

EPI to an existing clinical ssh-EPI protocol, while maintaining same scan times and an equivalent number of effective NSAs for b=1000 s/mm^2. Further investigation is needed to investigate the best parameter choice for clinical adoption. Importantly, our study did not include patient data. We only included healthy volunteers to assess the qualitative merits and quantitative accuracy of this novel approach, which is a limitation of the scope.

In this work, only one SPAIR fat-suppressed msh-EPI dataset is shown (see Figure 5), because a recent study did already demonstrate that SPAIR-msh-EPI helps to reduce the geometric distortion reduction compared to ssh-EPI[145]. That finding is strongly supported by the data of this work. However, roughly speaking, by adding this fat suppression (SPAIR increases the sampling time per slice by ~130 ms), the duration of one SPAIR-msh-EPI shot doubles compared to the Dixon-msh-EPI approach. This is an issue, because the in this study used protocols acquired only 12 slices at 3 mm thickness, which may not be sufficient for complete prostate coverage, indicating a need for either additional slices or thicker ones[139]. However, skipping the need for fat suppression, replacing it by Dixon, could improve the overall DWI sampling efficiency. A such extended coverage feasible with our approach will also be of interest for much more extended anatomies like the female breast.

In general, Dixon-msh-EPI offers a highly efficient alternative compared to ssh-EPI, since signal averaging is always required in low-SNR prostate DWI, providing a window of opportunity of making more use of repeated measurements than just averaging. For example, by adding a few milliseconds for chemical shift encoding, fat suppression based on Dixon comes for free when data must be re-acquired to enable signal averaging. Furthermore, due to its insensitivity to B_0 inhomogeneities compared to SPAIR, a smaller/precise shimming box could be used to focus on the prostate which will further reduce susceptibility effects. It should also be noted that, in this study no additional denoising was applied to the DWI data. AI-driven[103,161] or classical approaches[134,162] could potentially be considered for this purpose, because both the Dixon-msh-EPI and the ssh-EPI images were phase corrected and complex averaged to improve the SNR, allowing for subsequent complex postprocessing and bias-free ADC evaluation as shown.

7.5 Conclusion

In this work, we have proposed to use Dixon-msh-EPI as an alternative method to acquire prostate DWI data. The Dixon-msh-EPI approach showed quantitative consistency with the standard clinically used ssh-EPI protocol, regarding ADC mapping and overall image quality, but showed significantly reduced geometric distortions. The use of Dixon-msh-EPI may be further developed in the future to support fat signal-based motion compensation, to increase spatial resolution, and to use fat as additional information for future prostate cancer diagnosis and management.

Acknowledgement

We acknowledge the fruitful discussions on clinical prostate DWI with Dr. Martin Wasser. This work is part of the research program HTSM with project number 17104, which is partly financed by the Dutch Research Council (NWO).

References

1. Turkbey B, Rosenkrantz AB, Haider MA, et al. Prostate Imaging Reporting and Data System Version 2.1: 2019 Update of Prostate Imaging Reporting and Data System Version 2. *Eur Urol*. 2019;76(3).

2. Maurer MH, Heverhagen JT. Diffusion weighted imaging of the prostate-principles, application, and advances. *Transl Androl Urol*. 2017;6(3):490-498.

3. Skare S, Newbould RD, Clayton DB, Albers GW, Nagle S, Bammer R. Clinical Multishot DW-EPI Through Parallel Imaging With Considerations of Susceptibility, Motion, and Noise. *Magnetic resonance in medicine : official journal of the Society of Magnetic Resonance in Medicine / Society of Magnetic Resonance in Medicine*. 2007;57(5):881.

4. Giganti F, Kasivisvanathan V, Kirkham A, et al. Prostate MRI quality: a critical review of the last 5 years and the role of the PI-QUAL score. *British Journal of Radiology*. 2022;95(1131).

5. Hoeks CMA, Barentsz JO, Hambrock T, et al. Prostate cancer: Multiparametric MR imaging for detection, localization, and staging. *Radiology*. 2011;261(1).

6. Attenberger UI, Rathmann N, Sertdemir M, et al. Small Field-of-view single-shot EPI-DWI of the prostate: Evaluation of spatially-tailored two-dimensional radiofrequency excitation pulses. *Z Med Phys*. 2016;26(2).

7. Andersson JLR, Skare S, Ashburner J. How to correct susceptibility distortions in spin-echo echo-planar images: Application to diffusion tensor imaging. *Neuroimage*. 2003;20(2):870-888.

8. Usman M, Kakkar L, Kirkham A, Arridge S, Atkinson D. Model-based reconstruction framework for correction of signal pile-up and geometric distortions in prostate diffusion MRI. *Magn Reson Med*. 2019;81(3):1979-1992.

9. Jezzard P, Balaban RS. Correction for geometric distortion in echo planar images from B0 field variations. *Magn Reson Med*. 1995;34(1):65-73.

10. Munger P, Greller GR, Peters TM, Pike GB. An inverse problem approach to the correction of distortion in EPI images. *IEEE Trans Med Imaging*. 2000;19(7):681-689.

11. Jeong HK, Gore JC, Anderson AW. High-resolution human diffusion tensor imaging using 2-D navigated multishot SENSE EPI at 7 T. *Magn Reson Med*. 2013;69(3):793-802.

12. Chen N kuei, Guidon A, Chang HC, Song AW. A robust multi-shot scan strategy for high-resolution diffusion weighted MRI enabled by multiplexed sensitivity-encoding (MUSE). *Neuroimage*. 2013;72:41-47.

13. Atkinson D, Porter DA, Hill DLG, Calamante F, Connelly A. Sampling and reconstruction effects due to motion in diffusion-weighted interleaved echo planar imaging. *Magn Reson Med*. 2000;44(1).

14. Mani M, Jacob M, Kelley D, Magnotta V. Multi-shot sensitivity-encoded diffusion data recovery using structured low-rank matrix completion (MUSSELS). *Magn Reson Med*. 2017;78(2):494-507.

15. Tamada T, Kido A, Ueda Y, et al. Comparison of single-shot EPI and multi-shot EPI in prostate DWI at 3.0 T. *Sci Rep*. 2022;12(1):1-10.

16. An H, Ma X, Pan Z, Guo H, Lee EYP. Qualitative and quantitative comparison of image quality between single-shot echo-planar and interleaved multi-shot echo-planar diffusion-weighted imaging in female pelvis. *Eur Radiol*. 2020;30(4):1876-1884.

17. Wu W, Miller KL. Image formation in diffusion MRI: A review of recent technical developments. *Journal of Magnetic Resonance Imaging*. 2017;46(3):646-662.

18. Guo H, Ma X, Zhang Z, Zhang B, Yuan C, Huang F. POCS-enhanced inherent correction of motion-induced phase errors (POCS-ICE) for high-resolution multishot diffusion MRI. *Magn Reson Med*. 2016;75(1):169-180.

19. Mani M, Aggarwal HK, Magnotta V, Jacob M. Improved MUSSELS reconstruction for high-resolution multi-shot diffusion weighted imaging. *Magn Reson Med*. 2020;83(6):2253-2263.

20. Dai E, Mani M, McNab JA. Multi-band multi-shot diffusion MRI reconstruction with joint usage of structured low-rank constraints and explicit phase mapping. *Magn Reson Med*. 2023;89(1):95-111.

21. Hu Y, Levine EG, Tian Q, et al. Motion-robust reconstruction of multishot diffusion-weighted images without phase estimation through locally low-rank regularization. *Magn Reson Med*. 2019;81(2):1181-1190.

22. Hu Y, Wang X, Tian Q, et al. Multi-shot diffusion-weighted MRI reconstruction with magnitude-based spatial-angular locally low-rank regularization (SPA-LLR). *Magn Reson Med*. 2020;83(5):1596-1607.

23. Bae YJ, Choi BS, Jeong HK, Sunwoo L, Jung C, Kim JH. Diffusion-weighted imaging of the head and neck: Influence of fat-suppression technique and multishot 2D navigated interleaved acquisitions. *American Journal of Neuroradiology*. 2018;39(1):145-150.

24. Dong Y, Koolstra K, Riedel M, van Osch MJP, Börnert P. Regularized joint water–fat separation with B0 map estimation in image space for 2D-navigated interleaved EPI based diffusion MRI. *Magn Reson Med*. 2021;86(6):3034-3051.

25. Burakiewicz J, Charles-Edwards GD, Goh V, Schaeffter T. Water-fat separation in diffusion-weighted EPI using an IDEAL approach with image navigator. *Magn Reson Med*. 2015;73(3):964-972.

26. Udayasankar UK, Martin D, Lauenstein T, et al. Role of spectral presaturation attenuated inversion-recovery fat-suppressed T2-weighted MR imaging in active inflammatory bowel disease. *Journal of Magnetic Resonance Imaging*. 2008;28(5):1133-1140.

27. Grant KB, Agarwal HK, Shih JH, et al. Comparison of calculated and acquired high b value diffusion-weighted imaging in prostate cancer. *Abdom Imaging*. 2015;40(3):578-586.

28. Medved M, Soylu-Boy FN, Karademir I, et al. High-resolution diffusion-weighted imaging of the prostate. *American Journal of Roentgenology*. 2014;203(1):85-90.

29. Usman M, Kakkar L, Matakos A, Kirkham A, Arridge S, Atkinson D. Joint B0 and image estimation integrated with model based reconstruction for field map update and distortion correction in prostate diffusion MRI. *Magn Reson Imaging*. 2020;65(September 2019):90-99.

30. Dong Y, Riedel M, Koolstra K, van Osch MJP, Börnert P. Water/fat separation for self-navigated diffusion-weighted multishot echo-planar imaging. *NMR Biomed*. 2023;36(1):e4822.

31. Anzai Y, Lufkin RB, Jabour BA, Hanafee WN. Fat-suppression failure artifacts simulating pathology on frequency-selective fat-suppression MR images of the head and neck. *AJNR Am J Neuroradiol*. 1992;13(3):879.

32. Dong Y, Koolstra K, Li Z, Riedel M, Osch MJP van, Börnert P. Structured low-rank reconstruction for navigator-free water/fat separated multi-shot diffusion-weighted EPI. *Magn Reson Med*. Published online September 27, 2023.

33. Yu H, Reeder SB, Shimakawa A, Brittain JH, Pelc NJ. Field map estimation with a region growing scheme for iterative 3-point water-fat decomposition. *Magn Reson Med*. 2005;54(4):1032-1039.

34. Yu H, Shimakawa A, McKenzie CA, Brodsky E, Brittain JH, Reeder SB. Multiecho water-fat separation and simultaneous R*2 estimation with multifrequency fat spectrum modeling. *Magn Reson Med*. 2008;60(5):1122-1134.

35. Reeder SB, Wen Z, Yu H, et al. Multicoil Dixon Chemical Species Separation with an Iterative Least-Squares Estimation Method. *Magn Reson Med*. 2004;51(1):35-45.

36. Reeder SB, Pineda AR, Wen Z, et al. Iterative decomposition of water and fat with echo asymmetry and least-squares estimation (IDEAL): Application with fast spin-echo imaging. *Magn Reson Med*. 2005;54(3):636-644.

37. Hernando D, Kellman P, Haldar JP, Liang ZP. Robust water/fat separation in the presence of large field inhomogeneities using a graph cut algorithm. *Magn Reson Med*. 2010;63(1):79-90.

38. Stocker D, Manoliu A, Becker AS, et al. Image Quality and Geometric Distortion of Modern Diffusion-Weighted Imaging Sequences in Magnetic Resonance Imaging of the Prostate. *Invest Radiol*. 2018;53(4):200-206.

39. Sprenger T, Sperl JI, Fernandez B, Haase A, Menzel MI. Real valued diffusion-weighted imaging using decorrelated phase filtering. *Magn Reson Med*. 2017;77(2):559-570.

40. Prah DE, Paulson ES, Nencka AS, Schmainda KM. A simple method for rectified noise floor suppression: Phase-corrected real data reconstruction with application to diffusion-weighted imaging. *Magn Reson Med*. 2010;64(2).

41. Bourne RM, Bongers A, Chatterjee A, Sved P, Watson G. Diffusion anisotropy in fresh and fixed prostate tissue ex vivo. *Magn Reson Med*. 2016;76(2).

42. Man LC, Pauly JM, Macovski A. Multifrequency interpolation for fast off-resonance correction. *Magn Reson Med*. 1997;37(5):785-792.

43. Koolstra K, O'Reilly T, Börnert P, Webb A. Image distortion correction for MRI in low field permanent magnet systems with strong B0 inhomogeneity and gradient field nonlinearities. *Magnetic Resonance Materials in Physics, Biology and Medicine*. 2021;34(4):631-642.

44. Skare S, Hartwig A, Mårtensson M, Avventi E, Engström M. Properties of a 2D fat navigator for prospective image domain correction of nodding motion in brain MRI. *Magn Reson Med*. 2015;73(3):1110-1119.

45. Gallichan D, Marques JP, Gruetter R. Retrospective correction of involuntary microscopic head movement using highly accelerated fat image navigators (3D FatNavs) at 7T. *Magn Reson Med*. 2016;75(3).

46. Pruessmann KP, Weiger M, Scheidegger MB, Boesiger P. SENSE: Sensitivity encoding for fast MRI. *Magn Reson Med*. 1999;42(5):952-962.

47. Avants BB, Epstein CL, Grossman M, Gee JC. Symmetric diffeomorphic image registration with cross-correlation: Evaluating automated labeling of elderly and neurodegenerative brain. *Med Image Anal*. 2008;12(1):26-41.

48. Garyfallidis E, Brett M, Amirbekian B, et al. Dipy, a library for the analysis of diffusion MRI data. *Front Neuroinform*. 2014;8(FEB).

49. Dregely I, Margolis DAJ, Sung K, et al. Rapid quantitative T2 mapping of the prostate using three-dimensional dual echo steady state MRI at 3T. *Magn Reson Med*. 2016;76(6):1720-1729.

50. Liao C, Cao X, Cho J, Zhang Z, Setsompop K, Bilgic B. Highly efficient MRI through multi-shot echo planar imaging. Published online 2019:43.

51. Hu HH, Börnert P, Hernando D, et al. ISMRM workshop on fat-water separation: Insights, applications and progress in MRI. *Magn Reson Med*. 2012;68(2):378-388.

52. Van Roermund JGH, Hinnen KA, Tolman CJ, et al. Periprostatic fat correlates with tumour aggressiveness in prostate cancer patients. *BJU Int*. 2011;107(11):1775-1779.

53. Woo S, Cho JY eon, Kim SY oun, Kim SH yup. Periprostatic fat thickness on MRI: correlation with Gleason score in prostate cancer. *AJR Am J Roentgenol*. 2015;204(1):W43-W47.

54. Tan WP, Lin C, Chen M, Deane LA. Periprostatic Fat: A Risk Factor for Prostate Cancer? *Urology*. 2016;98:107-112.

55. Hernando D, Karampinos DC, King KF, et al. Removal of olefinic fat chemical shift artifact in diffusion MRI. *Magn Reson Med*. 2011;65(3):692-701.

56. Burakiewicz J, Hooijmans MT, Webb AG, Verschuuren JJGM, Niks EH, Kan HE. Improved olefinic fat suppression in skeletal muscle DTI using a magnitude-based dixon method. *Magn Reson Med*. 2018;79(1):152-159.

57. Hamilton G, Yokoo T, Bydder M, et al. In vivo characterization of the liver fat 1H MR spectrum. *NMR Biomed*. 2011;24(7):784-790.

58. Fadnavis S, Batson J, Garyfallidis E. Patch2Self: Denoising Diffusion MRI with Self-Supervised Learning. 2020;(NeurIPS):1-11. http://arxiv.org/abs/2011.01355

59. Kaye EA, Aherne EA, Duzgol C, et al. Accelerating Prostate Diffusion-weighted MRI Using a Guided Denoising Convolutional Neural Network: Retrospective Feasibility Study. *Radiol Artif Intell*. 2020;2(5):e200007.

60. Veraart J, Novikov DS, Christiaens D, Ades-aron B, Sijbers J, Fieremans E. Denoising of diffusion MRI using random matrix theory. *Neuroimage*. 2016;142:394-406.

61. Manjó N J V, Coupé P, Buades CL, Collins AL. Diffusion Weighted Image Denoising Using Overcomplete Local PCA. *PLoS One*. 2013;8(9):73021.